Available on the CERN CDS information server

CMS PAS EXO-21-007
TOTEM NOTE 2022-005

CMS Physics Analysis Summary

Contact: cms-pag-conveners-exotica@cern.ch

2022/05/23

Search for high-mass exclusive diphoton production with tagged protons

The CMS and TOTEM Collaborations

Abstract

A search for high-mass exclusive diphoton production via photon-photon fusion with tagged protons is presented. The analysis utilizes 102.7 fb^{-1} of data collected by the CMS and TOTEM Precision Proton Spectrometer in the 2016, 2017, and 2018 LHC runs. Events are selected that have two photons with high transverse momenta that are back-to-back in azimuth and with a large diphoton invariant mass. To remove the dominant backgrounds, tagged final state protons from the event are required to match the kinematics of the final state photons. Only events having opposite-side protons within an asymmetric fractional momentum loss between 0.035 and 0.15 (0.18) for the detectors on the negative (positive) side of CMS are considered. One exclusive diphoton candidate is observed for an expected background of 1.1 events. Limits at 95% confidence level are derived on the four-photon anomalous coupling parameters for $|\zeta_1| < 7.3 \times 10^{-14}$ GeV^{-4}, $|\zeta_2| < 1.5 \times 10^{-13}$ GeV^{-4} using an effective field theory. Additionally, axion-like particles are excluded in the mass range of 500 to 2000 GeV.

1 Introduction

While the Standard Model (SM) of particle physics has been largely successful in describing the universe, there are still many observed phenomena that suggest it is incomplete. Studying photon-photon interactions as part of the Light-by-Light (LbL) scattering process can provide theories that go beyond the standard model (BSM) by predicting the anomalous couplings of photons. Examples of these theories include composite Higgs [1], warped extra dimensions [2], and Kaluza-Klein gravitons [3]. The SM LbL process has been observed by both the CMS and ATLAS collaborations in heavy ion (HI) collisions [4–6], however, contributions to the four-photon (4γ) cross-section from BSM physics are expected at higher two-photon invariant masses than can be reached in HI collisions.

Using proton-proton (pp) collisions at the Large Hadron Collider (LHC), evidence for BSM physics can be probed at the electroweak scale. Furthermore, when two protons undergo an electromagnetic interaction at the LHC, the original protons can remain intact in the final state as seen in Figure 1. Measuring these final state protons gives the best sensitivity to study 4γ anomalous couplings [7].

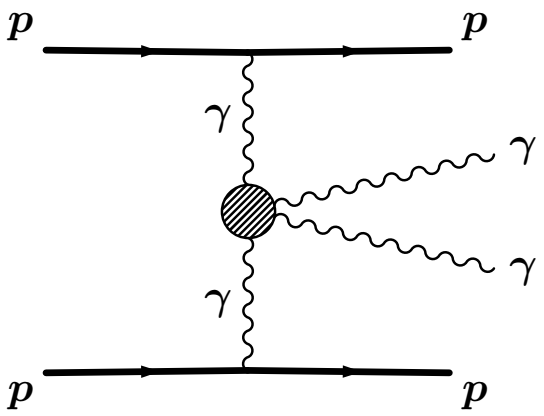

Figure 1: The process for diphoton production via photon exchange with intact protons in the final state. Several couplings may enter the four-photon shaded area such as a loop (box) of charged fermions or bosons. The model can be extended with intermediate interactions of new physics objects, such as a loop of a heavy charged particle or an s-channel process producing a scalar axion-like resonance that decays into two photons.

As has been shown in Ref. [7], with the assumption of a new mass scale heavier than the current reachable experimental energy, the 4γ interactions can be described by an effective Lagrangian using dimension-8 operators

$$\mathcal{L}_{4\gamma} = \zeta_1 F_{\mu\nu}F^{\mu\nu}F_{\rho\sigma}F^{\rho\sigma} + \zeta_2 F_{\mu\nu}F^{\nu\rho}F_{\rho\lambda}F^{\lambda\mu}. \tag{1}$$

These ζ_1 and ζ_2 parameters are identically zero in the SM, but in the case of a loop of a heavy charged particle or a resonance of a neutral particle, the contribution to the 4γ process would be nonzero.

From Equation 1, the angular cross-section of the four-photon interaction can be computed as

$$\frac{d\sigma}{d\Omega} = \frac{1}{16\pi^2 s}\left(s^2+t^2+st\right)^2\left[48\zeta_1^2 + 40\zeta_1\zeta_2 + 11\zeta_2^2\right]$$

where s and t are the Mandelstam variables.

Conversely, an s-channel production of a pseudo-scalar such as an axion-like particle (ALP) could give rise to an increased production rate of the LbL process when compared to the SM calculation [8]. ALP production is often characterized by the ALP mass and the electromagnetic coupling, f^{-1} as in Ref. [9].

The analysis strategy is to search for diphoton events exhibiting kinematics consistent with exclusive production in coincidence with two, opposite-side protons having a momentum loss equivalent to the momentum of the two photons.

With respect to the previous exclusive diphoton result reported by CMS [10], a set of new techniques are used to improve the sensitivity to the 4γ process. The new techniques include a more efficient photon identification algorithm, improved proton reconstruction, and a more robust background estimation.

2 The CMS detector and event reconstruction

This analysis relies equally on the central CMS detector and PPS as seen in Figure 2. Each of these are described below along with the event reconstruction algorithms.

2.1 The central CMS detector

The central feature of the CMS apparatus is a superconducting solenoid of 6 m internal diameter, providing a magnetic field of 3.8 T. Within the solenoid volume are a silicon pixel and strip tracker, a lead tungstate crystal electromagnetic calorimeter (ECAL), and a brass and scintillator hadron calorimeter (HCAL), each composed of a barrel and two endcap sections. Forward calorimeters extend the pseudorapidity coverage provided by the barrel and endcap detectors. Muons are detected in gas-ionization chambers embedded in the steel flux-return yoke outside the solenoid.

The electromagnetic calorimeter consists of 75 848 lead tungstate crystals, which provide coverage in pseudorapidity $|\eta| < 1.48$ in a barrel region (EB) and $1.48 < |\eta| < 3.0$ in two endcap regions (EE). Preshower detectors consisting of two planes of silicon sensors interleaved with a total of $3X_0$ of lead are located in front of each EE detector.

In the EB, an energy resolution of about 1% is achieved for unconverted or late-converting photons in the tens of GeV energy range. The remaining barrel photons have a resolution of about 1.3% up to a pseudorapidity of $|\eta| = 1$, rising to about 2.5% at $|\eta| = 1.4$. In the endcaps, the resolution of unconverted or late-converting photons is about 2.5%, while the remaining endcap photons have a resolution between 3 and 4% [11].

A more detailed description of the CMS detector, together with a definition of the coordinate system used and the relevant kinematic variables, can be found in Ref. [12].

Events of interest are selected using a two-tiered trigger system. The first level (L1), composed of custom hardware processors, uses information from the calorimeters and muon detectors to select events at a rate of around 100 kHz within a fixed latency of about 4 μs [13]. The second level, known as the high-level trigger (HLT), consists of a farm of processors running a version of the full event reconstruction software optimized for fast processing, and reduces the event rate to around 1 kHz before data storage [14].

The global event reconstruction (also called particle-flow event reconstruction [15]) aims to reconstruct and identify each individual particle in an event, with an optimized combination of all subdetector information. In this process, the identification of the particle type (photon,

electron, muon, charged hadron, neutral hadron) plays an important role in the determination of the particle direction and energy. Photons (e.g. coming from π^0 decays or from electron bremsstrahlung) are identified as ECAL energy clusters not linked to the extrapolation of any charged particle trajectory to the ECAL. Electrons are identified by a primary charged particle track and potentially many ECAL energy clusters corresponding to the extrapolation of this track to the ECAL as well as possible bremsstrahlung photons emitted along the way through the tracker material. Muons (e.g. from B hadron semileptonic decays) are identified as tracks in the central tracker consistent with either a track or several hits in the muon system, and associated with calorimeter deposits compatible with the muon hypothesis. Charged hadrons are identified as charged particle tracks that are not identified as electrons, nor as muons. Finally, neutral hadrons are identified as HCAL energy clusters not linked to any charged hadron trajectory, or as a combined ECAL and HCAL energy excess with respect to the expected charged hadron energy deposit.

The energy of photons is obtained from the ECAL measurement. The energy of electrons is determined from a combination of the track momentum at the main interaction vertex, the corresponding ECAL cluster energy, and the energy sum of all bremsstrahlung photons attached to the track. The energy of muons is obtained from the corresponding track momentum. The energy of charged hadrons is determined from a combination of the track momentum and the corresponding ECAL and HCAL energies, corrected for the response function of the calorimeters to hadronic showers. Finally, the energy of neutral hadrons is obtained from the corresponding corrected ECAL and HCAL energies.

For each event, hadronic jets are clustered from these reconstructed particles using the infrared and collinear safe anti-k_{T} algorithm [16, 17] with a distance parameter of 0.4. The jet momentum is determined as the vectorial sum of all particle momenta in the jet, and is found from simulation to be, on average, within 5 to 10% of the true momentum over the whole p_{T} spectrum and detector acceptance. Additional proton-proton interactions within the same or nearby bunch crossings (pileup) can contribute additional tracks and calorimetric energy depositions to the jet momentum. To mitigate this effect, charged particles identified to be originating from pileup vertices are discarded and an offset correction is applied to correct for remaining contributions. Jet energy corrections are derived from simulation to bring the measured response of jets to that of particle level jets on average. In situ measurements of the momentum balance in dijet, photon + jet, Z + jet, and multijet events are used to account for any residual differences in the jet energy scale between data and simulation [18]. The jet energy resolution amounts typically to 15–20% at 30 GeV, 10% at 100 GeV, and 5% at 1 TeV [18]. Additional selection criteria are applied to each jet to remove jets potentially dominated by anomalous contributions from various subdetector components or reconstruction failures.

2.2 The Precision Proton Spectrometer

The CMS Precision Proton Spectrometer (PPS) evolved out of a collaboration between the CMS and TOTEM experiments (previously named CT-PPS). The motivation for these detectors is to extend the CMS physics program to study central-exclusive production (CEP) processes in high-luminosity environments at the LHC both in the context of SM physics and BSM physics[19]. The PPS detectors are located 210 and 220 m away from the LHC interaction point 5 (IP5) on either side of CMS as seen in Figure 2.

After a pp collision at IP5, if a proton remains intact in the final state, it will continue to travel down the LHC beam line, guided by the LHC magnets, until it interacts with the PPS detectors in the forward regions. The horizontal distance of the proton from the center of the beam is

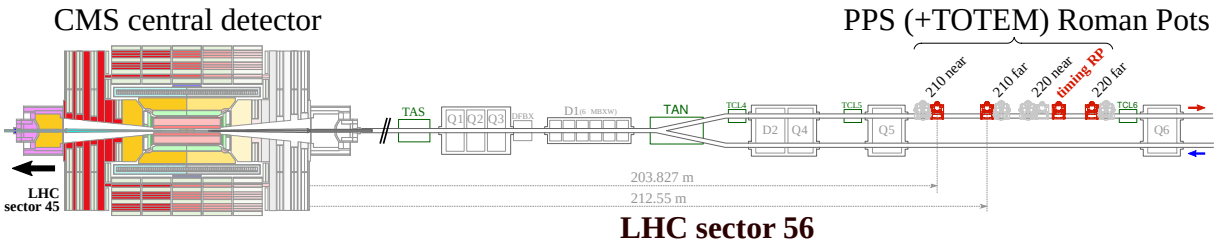

Figure 2: A schematic of one side of the PPS detector with respect to the central CMS detector. The 210 and 220 m stations are identified that house the Roman Pot detectors. Timing detector stations are also noted, but they are not used in this analysis. A symmetric set of detectors exists on the other side of CMS as well.

proportional to the momentum loss of the proton, and in this way, the LHC magnetic lattice acts as a mass spectrometer for measuring protons. The main observable used in analysis is the fractional momentum loss of the proton, denoted as ξ. When measuring each of the final state protons from an exclusive event, the two ξ values can be used to derive the mass and rapidity of the centrally produced system as follows:

$$m_{pp} = \sqrt{s\xi_p^+\xi_p^-}, \quad y_{pp} = \frac{1}{2}\log\left(\frac{\xi_p^+}{\xi_p^-}\right). \tag{2}$$

The PPS detectors located in the positive-z direction from CMS are referred to as sector-45 (for the area between interaction point 4 (IP4) and IP5), and the PPS detectors located in the negative-z direction from CMS are referred to as sector-56 (for the area between IP5 and IP6) as seen in Figure 2. At each of the 210 and 220 m stations, movable, near-beam insertions called Roman Pots (RPs) provide the housing for the proton tracking detectors.

A detailed description of the detector system, alignment, optics, and simulation are described in Ref. [20].

During the LHC Run 2 period, PPS collected over 110 fb^{-1} of data. Using 9.4 fb^{-1} of data from 2016, the first validation of the PPS system came through the observation of the SM process $\gamma\gamma \to \ell\ell$ [21]. Events were selected based on the lepton kinematics as well as proton kinematics that corresponded to the central system. This signal yield corresponds to a significance greater than 5.1σ and is the first observation of this process at the electroweak scale.

3 Data sets and simulated samples

This analysis uses pp data sets from the LHC Run 2 period collected by the CMS experiment in 2016, 2017, and 2018, corresponding to integrated luminosities of 9.8 [22], 37.2 [23], and 55.7 [24] fb^{-1}, respectively. The data sets are a convolution of the LHC running periods where all central CMS and PPS detectors were operating and included in the data acquisition.

Simulated samples are used to model the SM backgrounds and signal contributions for the study of the event selection. The dominant background is the inclusive $\gamma\gamma$+jet(s) sample where "jet(s)" are loosely classified as any radiation of energy. This sample is modelled at next-to-leading order (NLO) through the MADGRAPH5_AMC@NLO [25] package with NNPDF3.0 parton distribution functions (PDFs) at next-to-NLO accuracy [26]. The sub leading $\mathrm{t\bar{t}} + j$ and $V + \gamma$ samples are also modelled through the MADGRAPH5_AMC@NLO package where V represents a photon, W boson, or Z boson. The decay channel used in the aforementioned

samples is $Z \to \ell^+\ell^-$ and $W^\pm \to \ell^\pm\nu_\ell$. To estimate the QCD background, an electron and photon enriched QCD sample generated with PYTHIA 8 [27] and the CP5 underlying event tune [28]) is also utilized.

LbL signal samples are generated using the Forward Physics Monte Carlo (FPMC)[29] assuming collinear photon emission from both incoming protons. The photon fluxes from each proton are modelled using the Budnev et al. parameterization [30]. For the simulated conditions of each data taking year, multiple anomalous quartic gauge coupling (AQGC) signal samples are generated for representative ζ_1 and ζ_2 values. The AQGC signal kinematic distributions can be seen in Figure 3. Additionally, samples modeling the ALP production via an s-channel exchange are produced for twelve different ALP masses between the range of 500–2000 GeV where the analysis reaches the best sensitivity. These samples serve to derive the signal efficiency. Kinematics for the various ALP mass samples can be seen in Figure 4. These distributions are independent of f^{-1}. It should be noted that both types of signal, AQGC and ALP, have similar kinematics that are studied using the same event selection criteria.

All simulated samples are produced with the GEANT4 [31] simulation of the CMS detector response with the addition of standard CMS pileup conditions (as opposed to low-luminosity pileup conditions).

4 Photon identification and isolation

A multivariate analysis (MVA) utilizing a boosted decision tree (BDT) is used for identification (ID) and isolation of photons. This technique allows for the definition of a single discriminating variable for each photon candidate that is based on many variables that help discriminate prompt photons from backgrounds. The inputs into the BDT are shower shape variables, isolation variables, and quantities based on the shower and isolation of pileup present in the event [11], each of which are described in this paragraph. The $\sigma_{i\eta i\eta}$ variable is the spatial second-order moment of the photon candidate with respect to η [32]. The R_9 variable is calculated as the sum of the energy contained by the 3×3 matrix centered on the most energetic crystal in the supercluster (cluster of clusters) divided by the supercluster energy. Another version of the R_9 variable is calculated as the sum of the energy contained by the 3×3 matrix centered on the most energetic crystal in the supercluster divided by the energy contained in the 5×5 matrix. The $q_{\eta\phi}$ variable is the covariance of the single-crystal values in η and ϕ for the 5×5 array of crystals centered on the highest energy crystal. The S_4 variable is the energy contained by the most energetic 2×2 array of crystals (containing the seed crystal) divided by the energy of the supercluster. The BDT also considers the η and ϕ width of the electromagnetic shower. The photon isolation variables that are considered are based on the PF algorithm. The I_γ, I_{chg}, and I_n are obtained by summing the transverse momenta of the photons, charged hadrons, and neutral hadrons, respectively, inside an isolation region of radius ΔR in the (η,ϕ) plane around the photon candidate [32]. Other variables used as inputs are the raw supercluster energy and supercluster η of the photon candidate as well as the average energy density of the event. Specifically for photon candidates in the endcap, the preshower σ_η and preshower energy divided by the supercluster energy are inputted to the decision tree.

The BDT is trained on simulated $\gamma + j$ events. The photon candidates are required to pass a preselection of criteria. The criteria are specific to each of the four categories that the photon candidate can belong to based on its location and R_9. The preselection criteria are shown in Table 1 where I_{trk} is the tracker hollow cone isolation defined as the sum of the transverse momenta of all tracks inside a cone around the photon candidate.

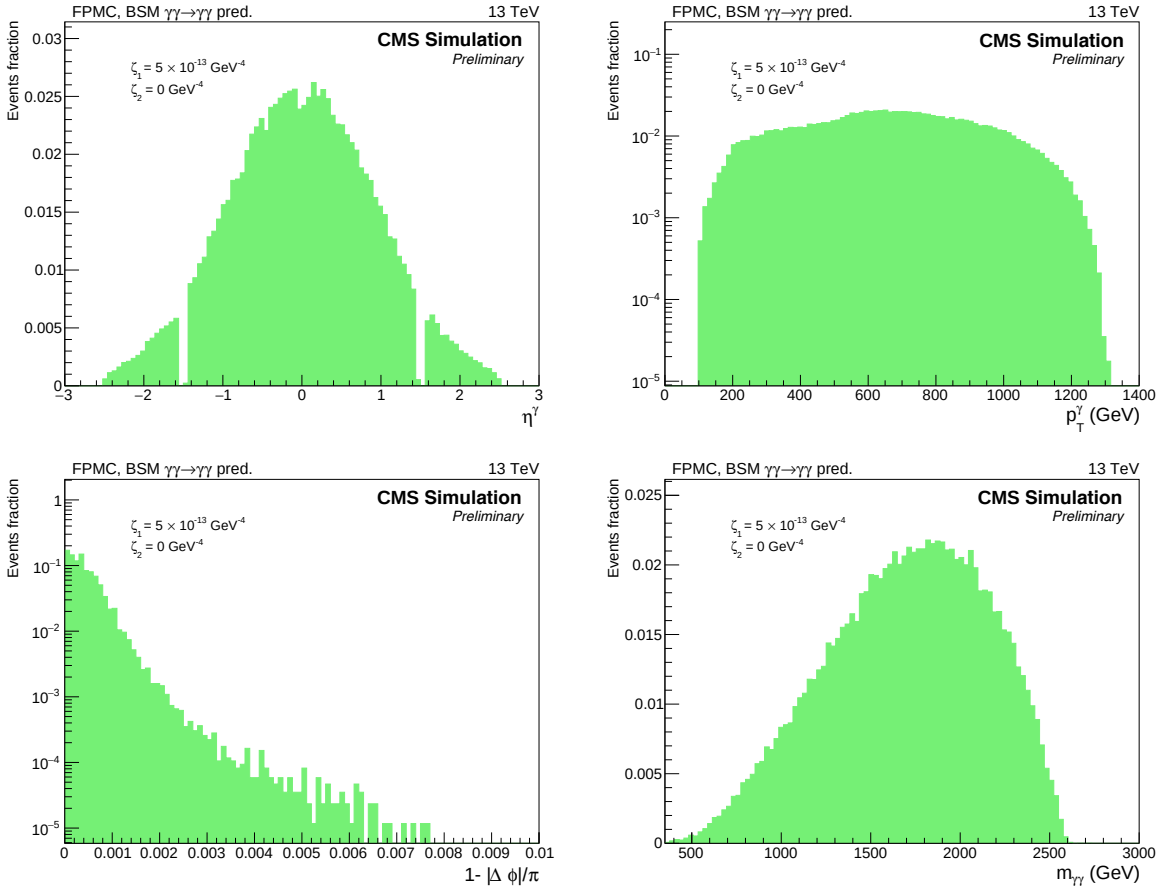

Figure 3: Anomalous Quartic Gauge Coupling (AQGC) signal kinematics for the single photon η (top left), single photon p_{T} (top right), diphoton acoplanarity (bottom left), diphoton mass (bottom right). The signal simulation shown here is generated with FPMC for an AQGC signal using $\zeta_1 = 5 \times 10^{-13}$ GeV $^{-4}$, $\zeta_2 = 0$ GeV $^{-4}$. The distributions represent the signal sample after undergoing the full CMS detector response. A preselection is applied to these events as described in Section 5.

A working point (WP) can be defined where the BDT output gives a signal efficiency of 90% for identifying photons. The corresponding BDT output for the working point giving a 90% signal efficiency (MVA WP90 ID) is found to be -0.02 for EB photons and -0.26 for EE photons.

The MVA ID makes identification and isolation requirements on the physics object in the CMS ECAL, but makes no prediction about whether the particle is a photon or an electron. For this reason, an electron veto is needed. An electron veto that is protected from converting photons is used to remove photon candidates that are actually electrons without removing converted photons. For the signal samples described in Section 3, the MVA ID is found to be 84.8% efficient, and the conversion-safe electron veto is found to be 96.2% efficient for the combination of both signal photons passing the ID.

5 Event selection

For the 2016 data the HLT trigger required a photon candidate to have a transverse momentum greater than 60 GeV and H/E[1] ratio below 0.15. For 2017 and 2018 the transverse momentum

[1]Defined as the ratio between the energy deposits in the hadronic and electromagnetic calorimeters

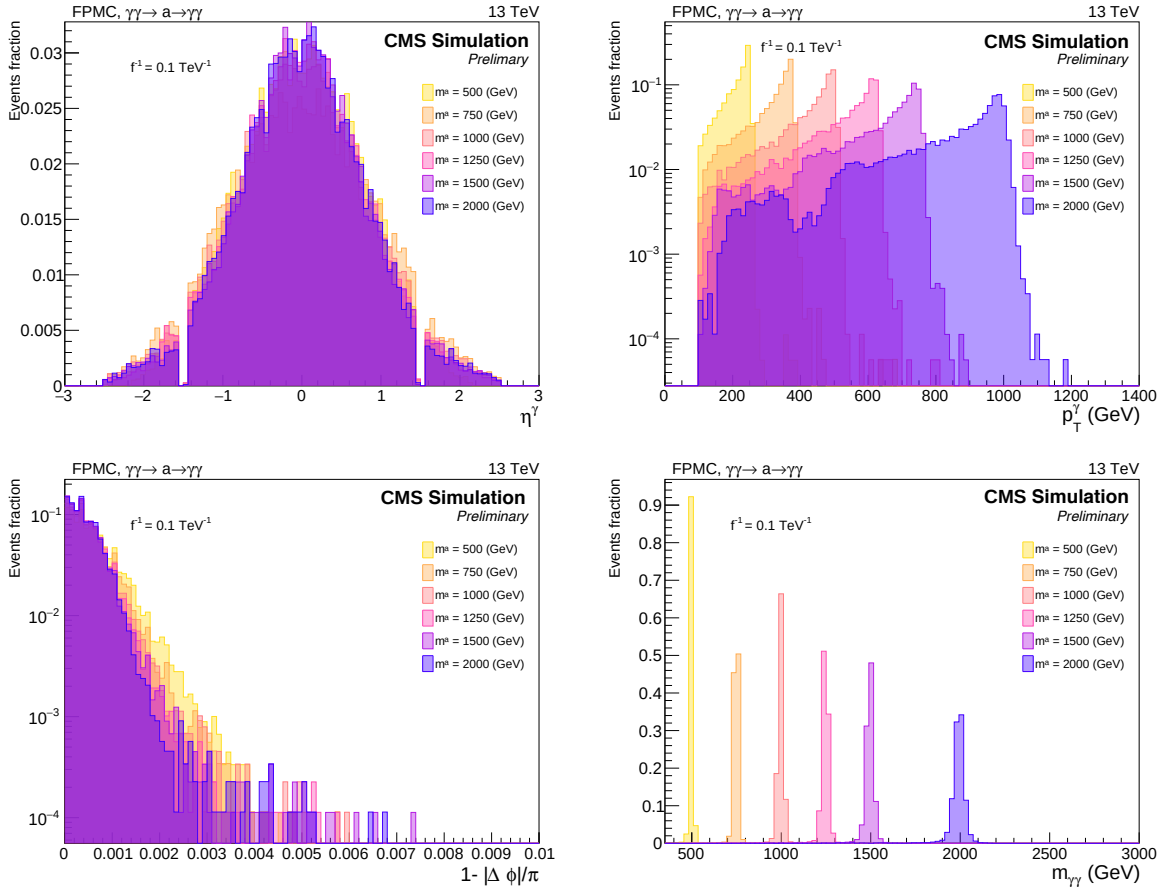

Figure 4: Axion-like particle (ALP) signal kinematics for the single photon η (top left), single photon p_{T} (top right), diphoton acoplanarity (bottom left), diphoton mass (bottom right). The signal simulation shown here is generated with FPMC for ALP signals using $f^{-1} = 10^{-1}$ TeV^{-1}. The distributions represent the signal sample after undergoing the full CMS detector response. A preselection is applied to these events as described in Section 5.

requirement was raised to 70 GeV. The efficiency of each of these triggers has been studied as a function of p_{T} and trigger-safe p_{T} selections are applied to the data. For the 2016 data, the trigger-safe p_{T} selection is placed at 75 GeV and, for the 2017 and 2018 data the p_{T} selection is placed at 100 GeV. Additionally, a trigger-safe H/E selection requirement of $H/E < 0.10$ is applied.

In addition to the HLT selection, the preselection makes selection criteria to ensure the quality of the selected events. To be sure that the electromagnetic objects selected by the trigger are photons, we use the MVA WP90 photon ID and conversion-safe electron veto described in section 4. Furthermore, the single photon pseudo-rapidity is constrained to be within the region $|\eta^{\gamma}| < 2.5$, with an additional veto between $1.4442 < |\eta^{\gamma}| < 1.566$, corresponding to the ECAL transition region between the barrel and the endcaps. The last requirement of the preselection is that the mass of the diphoton pair be greater than the 350 GeV where the SM LbL process is negligible as motivated in [33].

In order to select the exclusive $\gamma\gamma \to \gamma\gamma$ process, a criterion is applied to select photons that are back-to-back with respect to the angle ϕ. The variable of interest to define this criterion is the *acoplanarity* between the two photons, defined as

Table 1: Selection criteria for various training samples used to train the BDT to identify photons. H/E is defined as the ratio between the energy deposits in the hadronic and electromagnetic calorimeters.

	H/E	$\sigma_{i\eta i\eta}$	R_9 (5×5)	I_γ (GeV)	I_{trk} (GeV)
EB & $R_9 > 0.85$	< 0.08	-	> 0.5	-	-
EB & $R_9 \leq 0.85$	< 0.08	< 0.015	> 0.5	< 4.0	< 6.0
EE & $R_9 > 0.9$	< 0.08	-	> 0.8	-	-
EE & $R_9 \leq 0.9$	< 0.08	< 0.035	> 0.8	< 4.0	< 6.0

Table 2: Summary of the predicted number of events for each Standard Model background contributing to the $\xi \in PPS$ selection region. The uncertainties quoted are statistical only.

Sample	**Events**
Incl. $\gamma\gamma + j$	580 ± 41
Incl. $\gamma + j$	110 ± 22
Incl. $W\gamma$	4 ± 2
Incl. $Z\gamma$	2 ± 1
Incl. $t\bar{t} + j$	negligible
QCD	negligible
Total predicted	696 ± 47
Observed	735
Data/MC	1.06

$$a \equiv 1 - \mid \Delta\phi^{\gamma\gamma}/\pi \mid . \tag{3}$$

Requesting $a < 0.0025$ results in the rejection of major inclusive backgrounds.

The final step in the event selection requires a selection on the ξ variables of the diphoton system within CMS defined as

$$\xi^{\pm}_{\gamma\gamma} = \frac{1}{\sqrt{s}} \sum_{i=1}^{2} p_{\mathrm{T}}^{\gamma_i} e^{\pm\eta_{\gamma_i}}. \tag{4}$$

In the case of a truly exclusive scattering event, the ξ values of the two intact protons are directly correlated to the central photons in CMS. The corresponding ξ values for the diphoton system are based only on kinematics. Therefore, if events are required to have forward protons within the acceptance of PPS, the diphoton ξ values must also be within the PPS ξ acceptance range. The positive and negative diphoton ξ values correspond to the protons moving in the positive-z and negative-z directions. Various kinematic distributions for events passing all of the selection criteria can be found in Figure 5. Therefore, the diphoton candidate is required to have kinematics consistent with the PPS acceptance by satisfying $0.02 < \xi^{\pm}_{\gamma\gamma} < 0.20$.

A quantitative description of the simulated background and data events passing this selection can be seen in Table 2. The data to Monte Carlo (MC) agreement is shown for the sequential preselection, acoplanarity selection, and diphoton ξ selection in Figure 6. Good agreement is observed, especially in the final selection region.

In addition to the CMS photon selection criteria, it was found that placing a lower selection criterion on the proton ξ values of 0.035 decreases the background (discussed in Section 6.1) while not decreasing the signal efficiency. An asymmetric selection is placed on the upper end of the proton ξ spectrum motivated by the PPS acceptance in Run 2. These asymmetric

selection criteria are placed at 0.15 for sector-45 and 0.18 for sector-56.

Table 3: A summary of the selection regions defined in the text.

Region	Selection
Preselection	Double photon HLT $p_T^\gamma > 75$ (100) GeV for 2016 (2017-2018) $H/E < 0.10$ MVA WP90 photon ID with electron veto $\lvert\eta^\gamma\rvert < 2.5$ (transition veto) $m_{\gamma\gamma} > 350$ GeV
Exclusive selection	$a < 0.0025$
$\xi \in$ PPS	$0.02 < \xi^{\pm}_{\gamma\gamma} < 0.20$
Asymmetric ξ acceptance	$0.035 < \xi_{PPS} < 0.15$ (0.18) for sector-45 (sector-56)

6 Results

After all selection criteria as summarized in Table 3 are applied, a comparison between the forward diproton and central diphoton kinematics is performed. To reiterate, the analysis strategy is to look for an excess of events where the mass and rapidity of the diphoton and diproton systems match. This is done using the values calculated in Equation 2 and their associated uncertainties given by

$$\frac{\delta m_{pp}}{m_{pp}} = \delta y_{pp} = \frac{1}{2}\left(\frac{\delta\xi_p^+}{\xi_p^+} \oplus \frac{\delta\xi_p^-}{\xi_p^-}\right) \tag{5}$$

where δm_{pp}, δy_{pp}, and $\delta\xi_p^{\pm}$ represent the uncertainty on the diproton mass, uncertainty on the diproton rapidity, and uncertainty on the positive and negative proton ξ, respectively.

The window for an event to be considered matching is within 2σ of equivalence between the forward and central mass and rapidity. The criteria for this matching within 2σ of the uncertainties are

$$\left(m_{pp} - m_{\gamma\gamma}\right)/\sigma\left(m_{pp} - m_{\gamma\gamma}\right) < 2 \tag{6}$$

$$\left(y_{pp} - y_{\gamma\gamma}\right)/\sigma\left(y_{pp} - y_{\gamma\gamma}\right) < 2 \tag{7}$$

where $\sigma\left(m_{pp} - m_{\gamma\gamma}\right)$ and $\sigma\left(y_{pp} - y_{\gamma\gamma}\right)$ are the uncertainties on the differences between the diphoton and diproton mass and rapidity, respectively. These uncertainties are derived event-by-event.

Figure 7 shows events from data as a function of how closely they match (in terms of sigmas) in mass and rapidity. One event is observed within the 2σ matching window.

6.1 Background estimation

The signal region of the forward-central matching is expected to have contamination from pileup contributions. The overlapping of pileup protons detected in PPS with inclusively produced diphotons in CMS can lead to "accidental" forward central matching.

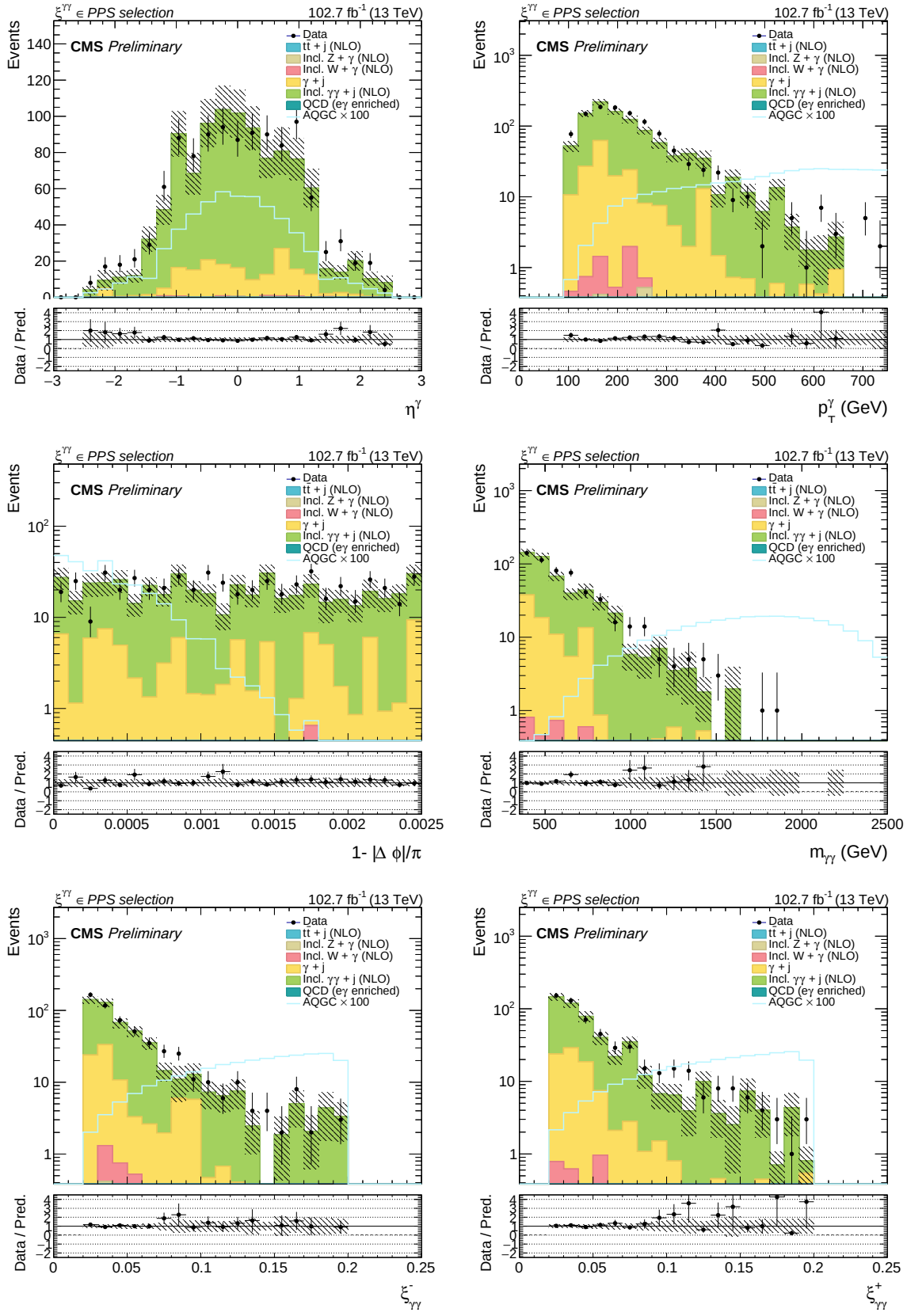

Figure 5: Kinematic distributions for events passing the $\xi^{\gamma\gamma} \in PPS$ signal selection. From top to bottom and left to right shows the single photon η, single photon p_{T}, diphoton acoplanarity, diphoton mass, diphoton ξ^{-}, and diphoton ξ^{+}. The black dots represent the data, filled histograms represent the SM backgrounds, and the lined histogram represents an AQGC signal having $\zeta_1 = 5\times10^{-13}$ GeV $^{-4}$ and $\zeta_2 = 0\times10^{-13}$ GeV $^{-4}$ multiplied by a factor of 100 for reference. The bottom of each plot shows the ratio of the number of data events to SM background events.

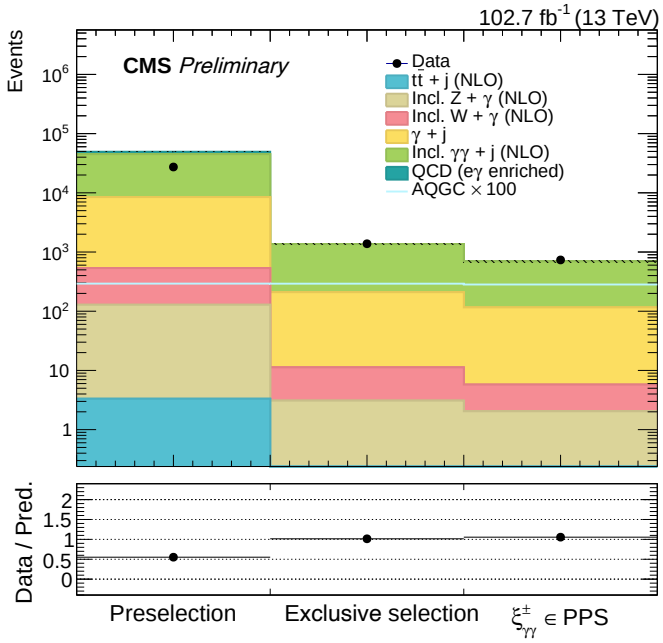

Figure 6: The number of data and simulated background events are shown for three sequential selection regions. The first bin is the preselection region, the second bin uses the acoplanarity selection defined in the text, and the third bin uses the diphoton ξ selection defined in the text.

To quantify how these events contaminate the signal region, we use a fully data-driven approach to creating toy events. As inputs for the creation of the toy events, diphoton events in the signal region are used as well as all protons from the Run 2 data taking period passing the diphoton trigger. Starting with the first diphoton pair, a set of protons are added to the two photons from the same run and LHC crossing-angle. We then check for the forward-central matching in mass and rapidity. This procedure is done for all of the diphoton events in the signal region to create one toy experiment. Since the protons are randomly mixed with the diphotons, any matching that occurs is truly accidental and not due to a true correlation between the forward and central systems. As expected, the number of matching events for the toy experiments follows a Poisson distribution. The background estimation is validated by using simulated diphoton events from the signal selection as an input to the toy experiment. In the same way, diphoton events from data from an orthogonal signal selection (reversing the acoplanarity selection) can also be used as an input to the toy experiments. Both validation methods give similar number of average matching events and are also used to extract a systematic uncertainty on the background estimation procedure.

The number of expected background events at 2σ is 0.030, 0.163, and 0.910 for 2016, 2017, and 2018, respectively. The total number of expected background events is 1.103 ± 0.003 (statistical). The difference in the background estimations between the years is driven by the luminosity, detector, and efficiency differences.

6.2 Systematic uncertainties

The integrated luminosities of the 2016, 2017, and 2018 data-taking periods are individually known with uncertainties in the 2.3–2.5% range [22–24], while the total Run 2 (2016–2018) integrated luminosity has an uncertainty of 1.8%, the improvement in precision reflecting the (uncorrelated) time evolution of some systematic effects. A 23.3%, 25.2%, and a 20.9% system-

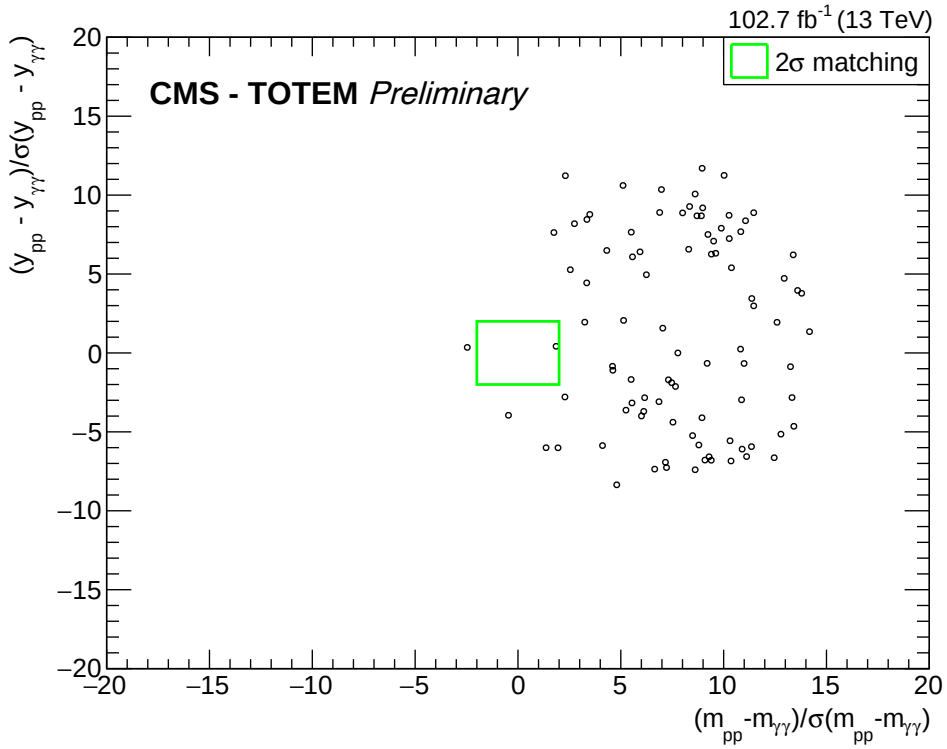

Figure 7: Mass and rapidity matching for events passing the CMS diphoton selection and two reconstructed protons passing the asymmetric proton ξ selection. Events matching at 2σ are enclosed within a green rectangle.

atic uncertainty on the background estimation procedure for 2016, 2017, and 2018, respectively, calculated as the largest relative difference in the number of estimated events between the default method and the two validation methods. For the signal efficiency in 2016, 2017, and 2018, a 3.1%, 7.0%, and 2.9% uncertainty are assigned, respectively, corresponding to the photon ID. A 10% uncertainty is assigned on the proton rapidity gap survival probability as done in [10] and calculated in [34]. A conservative 1.7% uncertainty is quoted on the particle showers in the PPS detectors in 2018. Systematic uncertainties on the proton reconstruction are assigned to protons on an event-by-event basis. All systematic uncertainties are applied to the signal except the uncertainty from the background estimation procedure. All systematic uncertainties are applied to the background except the uncertainty from the survival probability. The systematic uncertainties described above are summarized in Table 4. Systematic uncertainties are treated as uncorrelated across the years.

Table 4: Systematic uncertainties corresponding to each year of data used in the analysis.

Source	**2016**	**2017**	**2018**
CMS Luminosity	1.2%	2.3%	2.5%
Background estimation	23.3%	25.2%	20.9%
Photon ID scale factors	3.1%	7.0%	2.9%
Rapidity Gap Survival Probability	10%	10%	10%
Particle Showers in PPS	–	–	1.7%

6.3 Limit on anomalous quartic gauge couplings

With one event observed and 1.10 ± 0.24 (statistical + systematic) events expected in the Run 2 data, no excess is observed above the SM prediction. Therefore, limits are placed on the anomalous coupling parameters, ζ_1 and ζ_2.

The modified frequentist criterion CLs [35, 36] with the profile likelihood ratio test statistic modified for upper limits [37] and determined by pseudo-experiments is used to evaluate the observed and expected limits at 95% confidence level (CL) on the production cross section of AQGC LbL scattering within the fiducial region. The signal efficiency is evaluated over a wide range of the couplings parameters ζ_1 and ζ_2 using FPMC [29] and found approximately constant for each year in the search region.

The product of the efficiency (ϵ) and the acceptance (A) for the AQGC signal are quantified and used as an input to the limit setting tool. The efficiency and acceptance for the forward proton detectors to reconstruct signal protons as a function of the proton ξ can be seen in Figure 8. The reconstruction efficiency and acceptance is calculated as the ratio of the number of reconstructed protons to generated protons using a simulation of the forward proton detectors. This simulation accounts for the LHC beam parameters, detector configuration, and detector technology used over the full data taking period. The width of the 2016 reconstruction efficiency distribution is narrower than the other years because of a different physical location of the one of the two RPs used for tracking, limiting the overlapping ξ acceptance of the two tracking RPs in this year. The peak of the 2017 reconstruction efficiency is lower than the other years because of the inability of the silicon strip detectors to reconstruct multiple protons within one bunch crossing. This inefficiency was intensified in 2017 as compared to 2016 because of the increase in the LHC luminosity. The signal efficiency is best in 2018 because of the use of pixel detector technology in all RPs, which do not suffer from the inefficiency of tracking multiple protons.

The calculated efficiencies for each year can be seen in Table 5. Systematic uncertainties are included as a nuisance parameter in the likelihood with a log-normal probability density function.

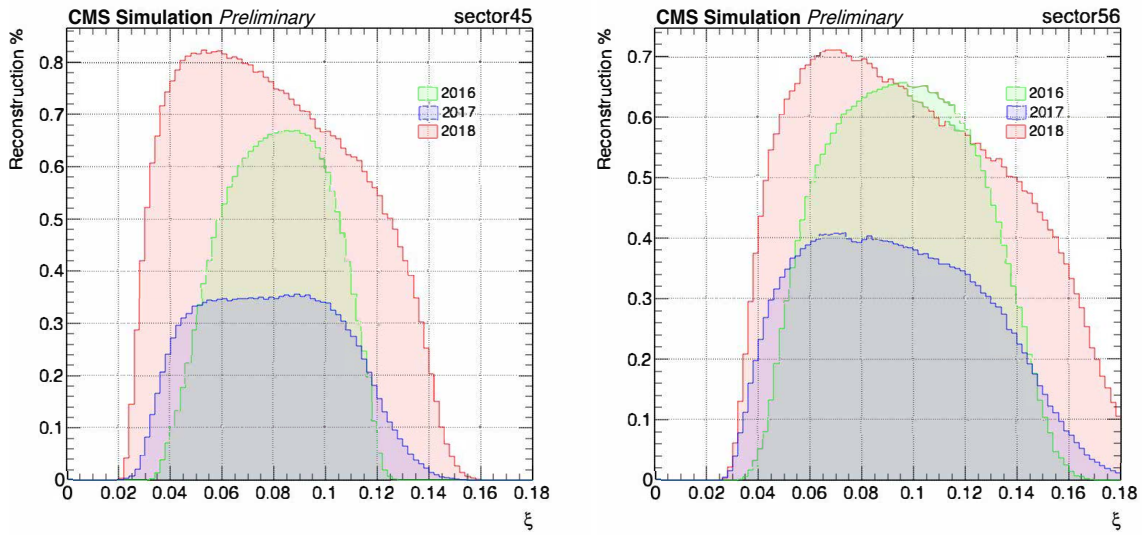

Figure 8: Both efficiency and acceptance effects parameterized as function of the proton ξ for all years. Differences in the reconstruction percentage can be attributed to differences in detector location, configuration, and design.

Table 5: Anomalous coupling signal efficiency for each year of the Run II period. The left column is the CMS only efficiency, the middle column is the PPS efficiency, and the right column is the multiplicative combination of the previous columns.

Year	CMS $\epsilon \times A$	PPS $\epsilon \times A$	$\epsilon \times A$
2016	80.1%	6.5%	5.2%
2017	75.7%	3.3%	2.5%
2018	77.4%	18.4%	14.2%

The observed (expected) limits on the coupling parameters (setting the other to be zero) are

$$
\begin{aligned}
|\,\zeta_1\,| &< 7.3(7.1) \times 10^{-14}\ \text{GeV}^{-4} \quad (\zeta_2 = 0), \\
|\,\zeta_2\,| &< 1.5(1.5) \times 10^{-13}\ \text{GeV}^{-4} \quad (\zeta_1 = 0).
\end{aligned}
$$

The observed and expected limits in the plane of (ζ_1, ζ_2) are shown in Figure 9.

These limits equate to the strongest upper limit on the anomalous four-photon coupling cross section of

$$\sigma(pp \to p\gamma\gamma p | \xi_p \in \xi^{\text{PPS}}) < 0.61 \text{ fb}. \tag{8}$$

6.4 Limit on axion-like particle production

The same limit setting procedure is applied to the s-channel production of a scalar axion-like particle. Following the approach described in [8], this $\gamma\gamma \to a \to \gamma\gamma$ process can be parameterized as a function of the ALP mass, m_{ALP}, and its coupling to the diphoton system, f^{-1}.

For the diphoton invariant mass acceptance determined by the ξ ranges probed in this analysis, the selection efficiency depends only on the mass of the ALP. The efficiency times acceptance, shown in Figure 10, are calculated for each sample and for each year and used as an input to the limit setting tool.

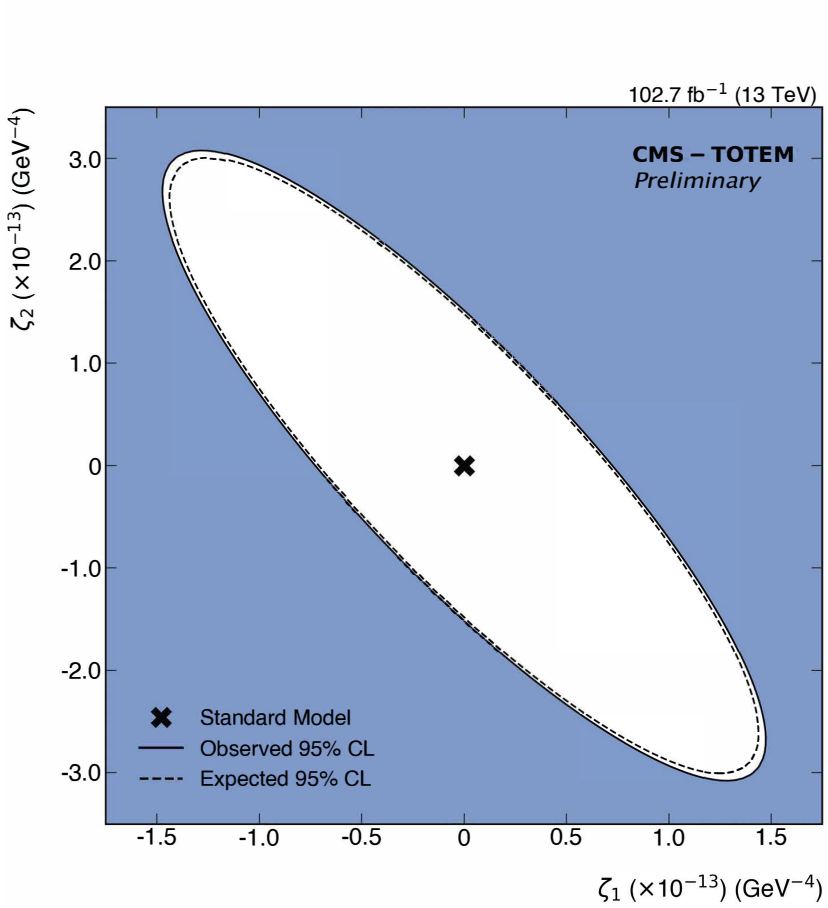

Figure 9: The observed and expected exclusion limits on the anomalous coupling parameters ζ_1 and ζ_2.

The observed and expected limits resulting from the analysis can be seen in Figure 11. These are the strongest limits for ALP masses in the range of 500 – 2000 GeV.

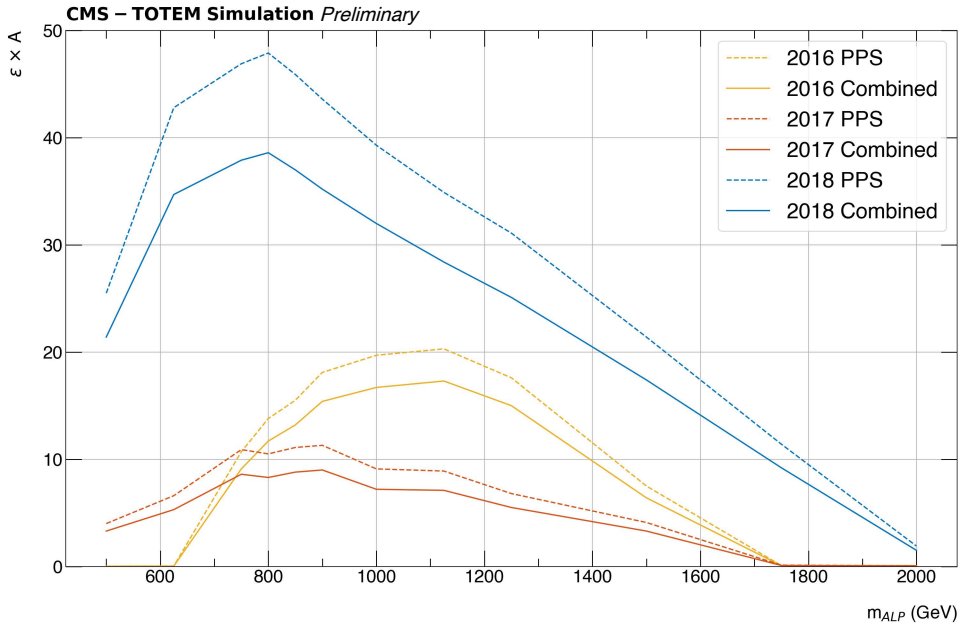

Figure 10: ALP signal efficiency times acceptance ($\epsilon \times A$) for samples generated with $f^{-1} = 10^{-1}$ TeV $^{-1}$ within the fiducial volume of this search. Values are shown for the PPS $\epsilon \times A$ and the same value convolved with the CMS $\epsilon \times A$. The CMS $\epsilon \times A$ remains mostly constant as a function of ALP mass and the nominal values are 85%, 80% and 81% for 2016, 2017, and 2018, respectively.

7 Summary

A search has been performed for physics beyond the standard model in high-mass exclusive diphoton events with two intact protons. The data used correspond to 102.7 fb^{-1} in pp collisions collected by the CMS and PPS detectors in 2016, 2017, and 2018. Signal diphoton events are selected using a criteria developed for exclusive two-photon production and the final signal region is defined by having two opposite-side protons with corresponding kinematics to the diphoton system.

The data are found to be in agreement with the predicted background with 1 event observed and 1.103 ± 0.003 (statistical) $\pm$ 0.238 (systematic) events expected. The best current limits are placed on 4γ anomalous couplings within the fiducial range of the analysis defined as $p_{\mathrm{T}}{}^{\gamma} > 100$ GeV and $0.035 < \xi < 0.15$ (0.18) for the positive-z (negative-z) arm of PPS. Additionally, the strongest limits to data are placed on ALP production between the mass ranges of 500 - 2000 GeV within the fiducial volume of the analysis.

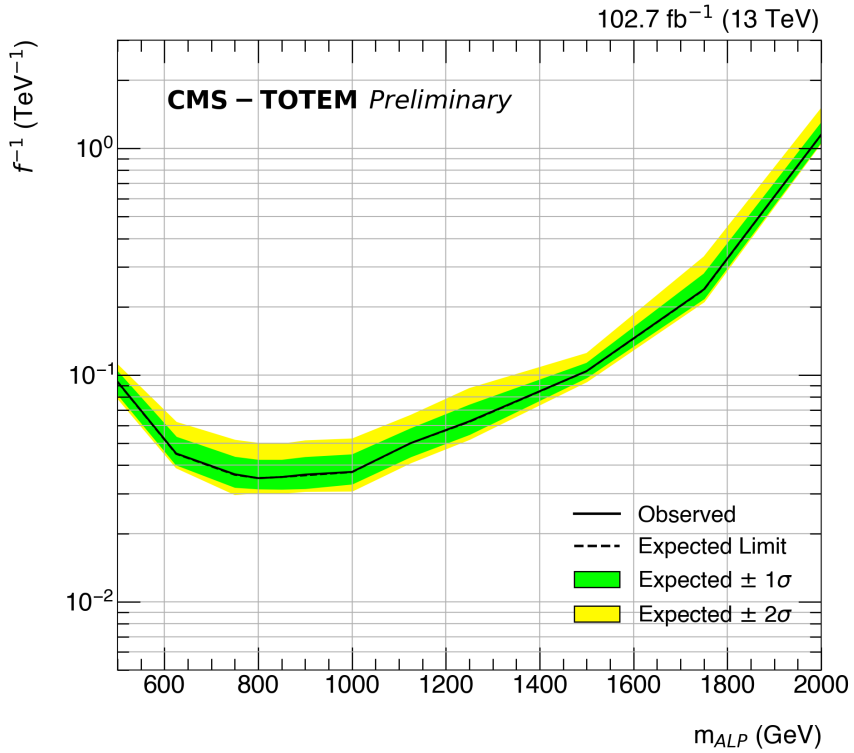

Figure 11: Limits on axion-like particle (ALP) production in the plane of the ALP mass and the coupling strength. The shape of the limit curve follows the PPS acceptance times efficiency curve.

References

[1] K. Agashe, R. Contino, and A. Pomarol, "The Minimal composite Higgs model", *Nucl. Phys. B* **719** (2005) 165–187, doi:10.1016/j.nuclphysb.2005.04.035, arXiv:hep-ph/0412089.

[2] K. Agashe, A. Delgado, M. J. May, and R. Sundrum, "RS1, custodial isospin and precision tests", *JHEP* **08** (2003) 050, doi:10.1088/1126-6708/2003/08/050, arXiv:hep-ph/0308036.

[3] L. Randall and R. Sundrum, "A Large mass hierarchy from a small extra dimension", *Phys. Rev. Lett.* **83** (1999) 3370–3373, doi:10.1103/PhysRevLett.83.3370, arXiv:hep-ph/9905221.

[4] ATLAS Collaboration, "Evidence for light-by-light scattering in heavy-ion collisions with the ATLAS detector at the LHC", *Nature Phys.* **13** (2017), no. 9, 852–858, doi:10.1038/nphys4208, arXiv:1702.01625.

[5] CMS Collaboration, "Evidence for light-by-light scattering and searches for axion-like particles in ultraperipheral PbPb collisions at $\sqrt{s_{\mathrm{NN}}} = 5.02$ TeV", *Phys. Lett. B* **797** (2019) 134826, doi:10.1016/j.physletb.2019.134826, arXiv:1810.04602.

[6] ATLAS Collaboration, "Observation of light-by-light scattering in ultraperipheral Pb+Pb collisions with the ATLAS detector", *Phys. Rev. Lett.* **123** (2019), no. 5, 052001, doi:10.1103/PhysRevLett.123.052001, arXiv:1904.03536.

[7] S. Fichet et al., "Light-by-light scattering with intact protons at the LHC: from Standard Model to New Physics", *JHEP* **02** (2015) 165, doi:10.1007/JHEP02(2015)165, arXiv:1411.6629.

[8] C. Baldenegro, S. Fichet, G. Von Gersdorff, and C. Royon, "Searching for axion-like particles with proton tagging at the LHC", *JHEP* **06** (2018) 131, doi:10.1007/JHEP06(2018)131, arXiv:1803.10835.

[9] M. Bauer, M. Neubert, and A. Thamm, "Collider Probes of Axion-Like Particles", *JHEP* **12** (2017) 044, doi:10.1007/JHEP12(2017)044, arXiv:1708.00443.

[10] CMS and TOTEM Collaborations, "First search for exclusive diphoton production at high mass with intact protons in proton-proton collisions at $\sqrt{s} = 13$ TeV at the LHC", Technical Report CMS-PAS-EXO-18-014, CERN, Geneva, 2020.

[11] CMS Collaboration, "Performance of photon reconstruction and identification with the CMS detector in proton-proton collisions at $\sqrt{s} = 8$ TeV", *JINST* **10** (2015) P08010, doi:10.1088/1748-0221/10/08/P08010, arXiv:1502.02702.

[12] CMS Collaboration, "The CMS experiment at the CERN LHC", *JINST* **3** (2008) S08004, doi:10.1088/1748-0221/3/08/S08004.

[13] CMS Collaboration, "Performance of the CMS Level-1 trigger in proton-proton collisions at $\sqrt{s} = 13$ TeV", *JINST* **15** (2020) P10017, doi:10.1088/1748-0221/15/10/P10017, arXiv:2006.10165.

[14] CMS Collaboration, "The CMS trigger system", *JINST* **12** (2017) P01020, doi:10.1088/1748-0221/12/01/P01020, arXiv:1609.02366.

[15] CMS Collaboration, "Particle-flow reconstruction and global event description with the CMS detector", *JINST* **12** (2017) P10003, doi:10.1088/1748-0221/12/10/P10003, arXiv:1706.04965.

[16] M. Cacciari, G. P. Salam, and G. Soyez, "The anti-k_t jet clustering algorithm", *JHEP* **04** (2008) 063, doi:10.1088/1126-6708/2008/04/063, arXiv:0802.1189.

[17] M. Cacciari, G. P. Salam, and G. Soyez, "FastJet user manual", *Eur. Phys. J. C* **72** (2012) 1896, doi:10.1140/epjc/s10052-012-1896-2, arXiv:1111.6097.

[18] CMS Collaboration, "Jet energy scale and resolution in the CMS experiment in pp collisions at 8 TeV", *JINST* **12** (2017) P02014, doi:10.1088/1748-0221/12/02/P02014, arXiv:1607.03663.

[19] CMS Collaboration, TOTEM Collaboration Collaboration, "Proton reconstruction with the CMS Precision Proton Spectrometer in Run 2", technical report, CERN, Geneva, 2022.

[20] CMS and TOTEM Collaborations, "Proton reconstruction with the Precision Proton Spectrometer in Run 2", Technical Report PRO-21-001, CERN, Geneva, 2021.

[21] CMS and TOTEM Collaborations, "Observation of proton-tagged, central (semi)exclusive production of high-mass lepton pairs in pp collisions at 13 TeV with the CMS-TOTEM precision proton spectrometer", *JHEP* **07** (2018) 153, doi:10.1007/JHEP07(2018)153, arXiv:1803.04496.

[22] CMS Collaboration, "CMS Luminosity Measurements for the 2016 Data Taking Period", Technical Report CMS-PAS-LUM-17-001, CERN, Geneva, 2017.

[23] CMS Collaboration Collaboration, "CMS luminosity measurement for the 2017 data-taking period at $\sqrt{s} = 13$ TeV", Technical Report CMS-PAS-LUM-17-004, CERN, Geneva, 2018.

[24] CMS Collaboration Collaboration, "CMS luminosity measurement for the 2018 data-taking period at $\sqrt{s} = 13$ TeV", Technical Report CMS-PAS-LUM-18-002, CERN, Geneva, 2019.

[25] J. Alwall et al., "The automated computation of tree-level and next-to-leading order differential cross sections, and their matching to parton shower simulations", *JHEP* **07** (2014) 079, doi:10.1007/JHEP07(2014)079, arXiv:1405.0301.

[26] NNPDF Collaboration, "Parton distributions for the LHC Run II", *JHEP* **04** (2015) 040, doi:10.1007/JHEP04(2015)040, arXiv:1410.8849.

[27] T. Sjöstrand et al., "An introduction to PYTHIA 8.2", *Comput. Phys. Commun.* **191** (2015) 159–177, doi:10.1016/j.cpc.2015.01.024, arXiv:1410.3012.

[28] CMS Collaboration, "Extraction and validation of a new set of CMS PYTHIA8 tunes from underlying-event measurements", *Eur. Phys. J. C* **80** (2020), no. 1, 4, doi:10.1140/epjc/s10052-019-7499-4, arXiv:1903.12179.

[29] M. Boonekamp et al., "FPMC: A Generator for forward physics", arXiv:1102.2531.

[30] V. M. Budnev, I. F. Ginzburg, G. V. Meledin, and V. G. Serbo, "The Two photon particle production mechanism. Physical problems. Applications. Equivalent photon approximation", *Phys. Rept.* **15** (1975) 181–281, doi:10.1016/0370-1573(75)90009-5.

[31] GEANT4 Collaboration, "GEANT4–a simulation toolkit", *Nucl. Instrum. Meth. A* **506** (2003) 250–303, doi:10.1016/S0168-9002(03)01368-8.

[32] CMS Collaboration, "Electron and photon reconstruction and identification with the CMS experiment at the CERN LHC", *JINST* **16** (2021), no. 05, P05014, doi:10.1088/1748-0221/16/05/P05014, arXiv:2012.06888.

[33] S. Fichet, G. von Gersdorff, and C. Royon, "Scattering light by light at 750 GeV at the LHC", *Phys. Rev.* **D93** (2016), no. 7, 075031, doi:10.1103/PhysRevD.93.075031, arXiv:1512.05751.

[34] L. A. Harland-Lang, V. A. Khoze, and M. G. Ryskin, "Exclusive physics at the LHC with SuperChic 2", *Eur. Phys. J. C* **76** (2016), no. 1, 9, doi:10.1140/epjc/s10052-015-3832-8, arXiv:1508.02718.

[35] T. Junk, "Confidence level computation for combining searches with small statistics", *Nucl. Instrum. Meth. A* **434** (1999) 435–443, doi:10.1016/S0168-9002(99)00498-2, arXiv:hep-ex/9902006.

[36] A. L. Read, "Modified frequentist analysis of search results (The CL(s) method)", in *Workshop on Confidence Limits*, pp. 81–101. 8, 2000.

[37] The ATLAS and CMS Collaborations and The LHC Higgs Combination Group, "Procedure for the LHC Higgs boson search combination in Summer 2011", Technical Report CMS-NOTE-2011-005. ATL-PHYS-PUB-2011-11, CERN, Geneva, Aug, 2011.